Electronic Supplementary Information

Organogelator design without solubilizing side chains by backbone contortion of perylene bisimide pigment

Zengqi Xie, Vladimir Stepanenko, Benjamin Fimmel and Frank Würthner*

Universität Würzburg, Institut für Organische Chemie & Center for Nanosystems Chemistry, Am Hubland, 97074 Würzburg, Germany

*E-mail: wuerthner@chemie.uni-wuerzburg.de

Table of Contents:

1. Materials and Methods

Solvents and reagents were purchased from commercial sources, unless otherwise stated, and purified and dried according to standard procedures. For UV/vis and fluorescence measurements spectroscopy grade solvents were used without further purification. FT-IR spectra were measured on a Jasco FT/IR-410 instrument at room temperature. Column chromatography was performed with silica gel (Merck Silica 60, particle size 0.035-0.070 mm). ^{1}H and ^{13}C NMR spectra were recorded on a 400 MHz spectrometer using tetramethylsilane (TMS) or residual solvent peak as internal standard. Mass spectra were performed on Bruker MALDI-TOF (autoflex II) and ESI-TOF (microTOF focus) instruments. UV/Vis spectra were recorded on a Perkin Elmer Lambda 40P spectrophotometer equipped with a Peltier system as temperature controller. Fluorescence emission spectra were recorded on a PTI QM4-2003 fluorescence spectrometer and were corrected against photomultiplier and lamp intensity. The fluorescence quantum yield in dichloromethane was determined using *N*,*N*'-bis(2,6-diisopropylphenyl)-1,6,7,12-tetraphenoxyperylene-3,4:9,10-tetracarboxylic acid bisimide (Φ_{fl} = 0.96 in $CHCl_3$) as the reference,[S1, S2] while the fluorescence quantum yield in MCH was determined by optical dilute method (OD < 0.05) under magic angle set up (54.7°) using nile blue A perchlorate (Φ_{fl} = 0.27 in EtOH at 24 °C)[S3] as the reference. AFM measurements were performed under ambient conditions using a Bruker AXS Multimode Nanoscope IV system operating in tapping mode in air. Silica cantilevers (OMCL-AC160TS) with a resonance frequency of ~300 kHz were used. TEM measurements were performed on a Siemens Elmiskop 101 Electron Microscope, operating at an acceleration voltage of 80 kV. SEM images of the sample on silica were taken using a FEI Helios Nanolab scanning electron microscope operated at 2 kV. High resolution TEM images and Selected Area Electron Diffraction (SAED) pattern were obtained with a FEI Titan 80-300 transmission electron microscope at an accelerating voltage of 300 kV. For X-ray powder diffraction we used a Bruker D8 Discover powder diffractometer (Cu-Kα radiation, unsplit Kα_1+Kα_2 doublet, mean wavelength λ = 154.19 pm). Samples were prepared on a silicon single crystal specimen holder. Detection was done with a LynxEye-1D-Detector.

For the data reported for PBI **4a** in MCH (e.g. Fig. 1) we like to note that this dye is actually not soluble in pure MCH. To prepare the aggregates in MCH we dissolved a tiny amount of PBI **4a** in dichloromethane to give a concentrated solution that was subsequently injected into a larger volume of MCH (usually several µL in CH_2Cl_2 were injected into 3 mL MCH), to get a suspension. The

suspension was then treated by supersonication to obtain a homogenous solution, which is stable for more than one hour without any precipitation (as confirmed by repetitive measurements of photoluminescence and UV/Vis absorption which do not show any contribution by light scattering, indicating that the size of the aggregates is smaller than the wavelength).

2. Synthesis

Synthesis of PBI **2a**. A portion of 0.30 g (0.41 mmol) compound **1**, 0.29 g (2.70 mmol) *o*-cresol and 0.17 g (1.35 mmol) K_2CO_3 were suspended in 10 mL NMP and stirred under argon at 140 °C for 20 hours. After being cooled to room temperature, the reaction mixture was dropped into 150 mL 1 N HCl under stirring. The solid was separated by filtration, and then washed successively with water (3×30 mL) and methanol (3×30 mL). The crude product was purified by column chromatography on silica gel using CH_2Cl_2/*n*-hexane (5:2) as an eluent. After removing the solvent with rotator evaporator, 0.30 g (yield: 72%) compound **2a** was collected as a deep red solid. ^{1}H NMR (400 MHz, $CDCl_3$, ppm): δ = 8.01 (s, 4H), 7.43 (d, ^2J = 7.7 Hz, 4H), 7.28 (t, ^2J = 7.2 Hz, 4H), 7.25-7.14 (m, 6H), 7.03-6.97 (m, 8H), 6.90-6.87 (m, 4H), 6.45 (q, ^3J = 7.3 Hz, 2H), 2.05(s, 12H), 1.91 (d, ^3J = 7.1 Hz, 6H). ^{13}C NMR (100 MHz, $CDCl_3$, ppm): δ = 163.6, 156.4, 153.3, 140.8, 133.2, 131.6, 130.0, 128.3, 127.6, 127.1, 125.2, 122.9, 120.6, 120.1, 119.5, 119.1, 50.3, 16.2. HRMS (ESI, $CHCl_3$/acetonitrile 1:1, pos mode): *m/z* calcd for $C_{68}H_{50}N_2O_8$: 1022.3567 $[M]^+$; found: 1022.3562. Elemental analysis: calcd (%) for $C_{68}H_{50}N_2O_8$: C 79.83, H 4.93, N 2.74; found: C 79.41, H 5.17, N 2.85.

Synthesis of PBI **2b**. A portion of 2.00 g (2.72 mmol) PBI **1**, 3.70 g (8.16 mmol) phenol and 0.56 g (4.08 mmol) K_2CO_3 were suspended in 25 mL NMP and stirred under argon at 130 °C for 19 h. After being cooled to room temperature, the reaction mixture was dropped into 120 mL 1 N HCl under stirring. The solid was separated by filtration, and then washed successively with water (3×20 mL) and methanol (3×20 mL). The crude product was purified by column chromatography on silica gel using CH_2Cl_2/*n*-hexane (80:20) as an eluent. After removing the solvent with rotator evaporator, 1.00 g (yield: 76%) compound **2b** was collected as a red solid. ^{1}H NMR (400 MHz, $CDCl_3$, ppm): δ = 8.15 (s, 4H), 7.42 (d, ^3J = 7.7 Hz, 4H), 7.32-7.18 (m, 14H), 7.09 (t, ^3J = 7.5Hz, 4H), 6.92 (2, ^3J = 7.9 Hz, 8H), 6.45 (q, ^3J = 7.1 Hz, 2H) 1.91 (d, ^3J = 7.1 Hz, 6H). ^{13}C NMR (100 MHz, $CDCl_3$, ppm):

δ = 163.3, 156.0, 155.2, 140.6, 132.8, 130.0, 128.1, 127.0, 124.6, 122.9, 120.4, 120.1, 120.0, 119.7, 50.2, 16.1. Elemental analysis: calcd (%) for $C_{64}H_{42}N_2O_8$: C 79.49, H 4.38, N 2.90; found: C 79.38, H 4.49, N 3.04.

Synthesis of perylene bisanydride **3a**. A portion of 245 mg (0.24 mmol) of perylene bisimide **2a** and 1.8 g (32 mmol) KOH solid were suspended in 20 mL *t*-BuOH and heated to 80 °C for 1.5 h. After being cooled to room temperature, the reaction mixture was dropped into 50 mL glacial acetic acid under stirring. Then 200 mL water was added to dilute the mixture. The solid was separated by filtration and washed with water (3×30 mL). The crude product (190 mg, yield 97%) was dried in vacuum (10^{-3} m bar, SiO_2) and was used for the next step without further purification. ^{1}H NMR (400 MHz, d_6-DMSO, ppm): δ = 7.71 (s, 4H), 7.35 (m,4H), 7.17 (m, 8H), 6.98 (m, 4H), 2.05 (s, 12H). ^{13}C NMR (100 MHz, $CDCl_3$, ppm): δ = 159.9, 156.8, 152.9, 133.9, 132.0, 130.0, 127.9, 125.8, 121.4, 121.0, 120.52, 120.47, 119.0, 16.2. HRMS (ESI, $CHCl_3$/acetonitrile 1:1, pos mode): *m/z* calcd for $C_{52}H_{33}O_{10}$: 817.2074 $[M+H]^+$; found: 817.2068. Elemental analysis: calcd (%) for $C_{52}H_{32}O_{10}$: C 76.46, H 3.95; found: C 76.20, H 4.25.

Synthesis of perylene bisanhydride **3b**. A portion of 0.50 g (0.52 mmol) of perylene bisimide **2b** and 2.9 g (51.6 mmol) KOH solid were suspended in 25 mL *t*-BuOH and heated to 80 ^{0}C for 10 h. After being cooled to room temperature, the reaction mixture was dropped into 90 mL glacial acetic acid under stirring. Then 150 mL water was added to dilute the mixture. The solid was separated by filtration and washed with water (3×30 mL). The crude product was purified by a flash column using CH_2Cl_2 as an eluent. After removing the solvent with rotator evaporator, 0.27 g (yield: 68.7%) of compound **3b** was obtained as a deep red solid. ^{1}H NMR (400 MHz, d_6-DMSO, ppm): δ = 7.87 (s, 4H), 7.40 (m, 8H), 7.23 (m, 4H), 7.04 (m, 8H).

Synthesis of target PBI **4a**. A solution of 163 mg (0.20 mmol) **3a** and 3.2 g ammonium acetate in 30 mL propionic acid was stirred at 140 °C for 12 h. After being cooled to room temperature, the mixture was dropped into 250 mL water under stirring. The precipitated solid was separated by filtration. The crude product was purified by precipitation by adding methanol into its concentrated solution in chloroform. After filtration and drying under vacuum (70 °C, 10^{-3} mbar, SiO_2), 140 mg

(yield: 86%) pure product was obtained. M.p. 448 °C.^{1}H NMR (400 MHz, d_6-DMSO, ppm): δ = 11.88 (s, 2H), 7.71 (s,4H), 7.31 (m, 4H), 7.13 (m, 8H), 7.25 (m, 4H), 6.98 (m, 4H), 2.05 (s, 12H). ^{13}C NMR (100 MHz, $CDCl_3$, ppm): δ = 163.3, 155.5, 152.8, 132.8, 131.5, 129.6, 127.6, 125.2, 123.1, 120.3, 119.8, 118.7, 116.7, 15.6. HRMS (ESI, $CHCl_3$/acetonitrile 1:1, pos mode): *m/z* calcd for $C_{52}H_{34}N_2O_8$: 814.2315 $[M]^+$; found: 814.2310. UV/vis (toluene): λ_{max} (ε_{max}) = 568 nm (42800), 530 nm (24900), 439 (14000). Fluorescence (CH_2Cl_2): λ_{max} = 606 nm (λ_{ex} = 530 nm), Φ_{fL} = 0.93±0.03. Elemental analysis: calcd (%) for $C_{52}H_{34}N_2O_8$: C 76.65, H 4.21, N 3.44; found: C 76.36, H 4.23, N 3.58.

Synthesis of compound **4b**. A solution of 190 mg (0.25 mmol) **3b** and 4.0 g ammonium acetate in 65 mL propionic acid was stirred at 140 °C for 20 hours. After cooled to room temperature, the mixture was dropped into 250 mL water under stirring. The precipitated solid was separated by filtration. Part of the crude product was purified by column chromatography using CH_2Cl_2/ethyl acetate (95:5) as an eluent. After removal of the solvent and drying under vacuum (70 °C, 10^{-3} mbar, SiO_2), 10 mg pure product was obtained. ^{1}H NMR (400 MHz, d_6-DMSO, ppm): δ = 11.93 (s, 2H), 7.86 (s, 4H), 7.38 (t, ^{3}J = 8.0 Hz, 8H), 7.20 (t, ^{3}J = 7.6 Hz, 4H), 7.03 (m, 8H). These data are in accordance with those reported in the literature for this compound (obtained by another synthetic route).[S4]

3. Temperature-Dependent UV/vis Spectra of 4a in Toluene: Evidence for Nucleation-Elongation Growth Mechanism

To elucidate the mechanism for the gel-sol transition temperature-dependent UV/vis spectroscopy of gelator **4a** in toluene at a concentration of 3.0×10^{-4} M was performed (Fig. S1). For this purpose, **4a** was dissolved in toluene by gentle heating and then the temperature was decreased to 10 °C to obtain the self-assembled J-aggregates. The absorption of the aggregate formed at 10 °C showed the characteristic J-band at around 650 nm (compare also Fig. 1), which decreased rapidly with increasing temperature. Concomitantly, the absorption band located at around 568 nm appeared which corresponds to the absorption of the molecularly dissolved **4a**. Three well-defined isosbestic points were observed at 588, 482 and 450 nm. The changes of the absorption at 650 nm and 568 nm were plotted versus temperature and the two curves obtained by sigmoidal fit intersect at 50 °C (see Fig. S1a inset) that is the decomposition temperature of **4a** aggregate in toluene, also called as "gel melting temperature". The absorption around 650 nm is assigned as the J-band of the aggregate, which exhibits a pronounced bathochromic shift of 82 nm compared with the absorption band of **4a** monomer solution in toluene, similarly as observed for a related dye bearing twelve dodecyloxy chains for solubilization.[S5]

The reversible formation of J-aggregates could also be confirmed by concentration-dependent UV/vis studies as shown in Figure S1b. With an increase of the concentration, the aggregates were formed and, correspondingly, the absorption band at around 650 nm emerged. Based on the concentration-dependent UV/vis spectra, the intensity of the molar absorbance at 650 nm was extracted and plotted versus the total concentrations (c_T) of all the dyes. To get further insight into the self-assembly mechanism the fraction of aggregated molecules (α_{agg}) was plotted as a function of Kc_T ($K = K_3 = K_4 \ldots$, is the equilibrium constant for elongation) with different σ values ($\sigma = K_2/K$, K_2 is the equilibrium constant for dimerization) as shown in the inset of Figure S1b. In the cooperative nucleation-growth model it is assumed that the equilibrium constant for the formation of the nucleation is smaller than that of the elongation. The simplest version of this model has only one dimerization step of nucleation, followed by isodesmic elongation steps. This means, only the dimerization (with equilibrium constant K_2) differs energetically relative to the following steps ($K_2 < K_3 = K_4 \ldots = K_i = \ldots = K$). This relation can be mathematically described as a cubic function presented in eqn (S1):

$$\alpha_{mon}^{3}(Kc_T)^2(\sigma-1)+\alpha_{mon}^{2}Kc_T(Kc_T-2(\sigma-1))-\alpha_{mon}(2Kc_T+1)+1=0 \quad \text{(S1)}$$

for a nucleus consisting of a dimer and $\sigma = K_2/K$. Even though it is not possible to solve eqn (S1) for a α_{mon} as a function of Kc_T for general cases, one can easily calculate Kc_T as a function of Kc_{mon} for certain σ values by using eqn (S2). From the obtained values α_{agg} can be calculated by using eqn (S3),

$$Kc_T=(1-\sigma)Kc_{mon}+\frac{\sigma Kc_{mon}}{(1-Kc_{mon})^2} \quad \text{(S2)}$$

$$\alpha_{agg}=1-\alpha_{mon}=1-\frac{Kc_{mon}}{Kc_T} \quad \text{(S3)}$$

and then α_{agg} can be plotted versus the corresponding Kc_T values, which is shown in the inset of Figure S1b. The curve for $\sigma < 1$ corresponds to the cooperative aggregation process.

Similar to our recently reported J-aggregates of core-substituted perylene bisimides equipped with a considerable number of alkyl side chains,[S5] also for PBI **4a** a nucleation-elongation mechanism was confirmed by this analysis. For PBI **4a** the values for K_2, K, and σ in toluene solvent were estimated to be 2-200 M^{-1}, $(2.1\pm0.2)\times10^4$ M^{-1}, and 10^{-2}-10^{-4}, respectively.

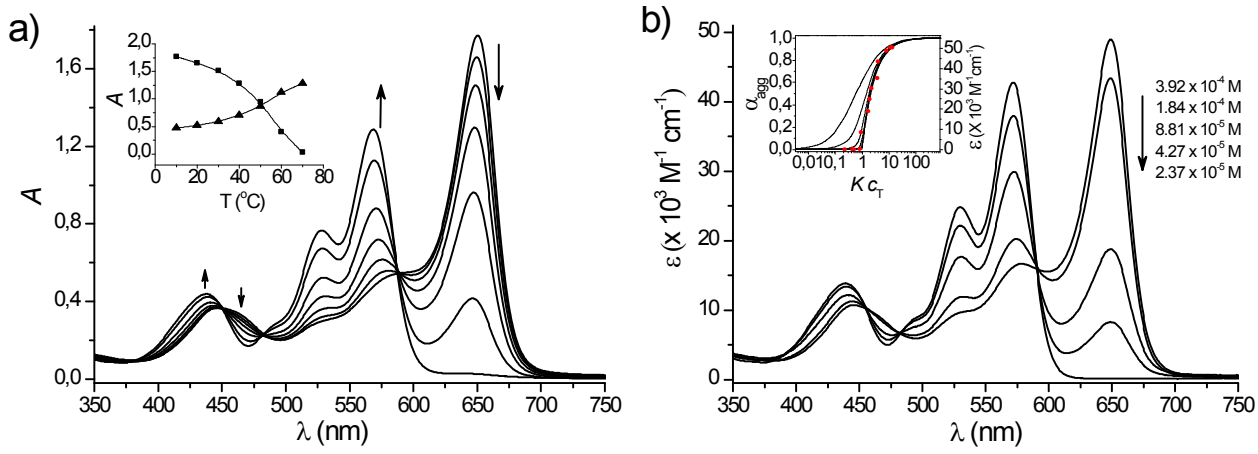

Fig. S1 (a) Temperature-dependent UV/vis spectra of **4a** in toluene from 10 to 70 °C at a concentration of 3.0×10^{-4} M in a 1 mm cell. Arrows indicate the spectral changes with increasing temperature. Inset shows the changes of absorption at 650 nm (■) and 568 nm (▲) upon increasing temperature and calculated lines according to sigmoidal fit. (b) Concentration-dependent UV/vis spectra of **4a** at 23 °C in toluene. The concentrations were determined from the absorption at 60 °C (molecularly dissolved) according to the molar absorbance coefficient. Inset shows the fraction of aggregated molecules α_{agg} plotted as a function of Kc_T with different σ values according to

cooperative nucleation-elongation model (lines from left to right: σ = 1, 0.1, 0.01, 0.001, 0.0001 and 0.00001), and plot of experimental absorption data of 4a in toluene (c = 1.1×10^{-6} to 6.3×10^{-4} M^{-1}) at 650 nm (●) after manual fit to the line shape.

4. Temperature-Dependent UV/vis Spectra of 4a in 1,2-Dichloroethane without and with Polystyrene in the Solution

The most obvious feature of the gelator **4a** is that there is no long alkyl chain in the molecular structure. The alkyl-chain-free structure of **4a** endows it a strong self-assembly ability to form one-dimensional nanofibers even in the presence of high concentration of polystyrene (PS). Figure S2 depicts the temperature-dependent UV/vis absorption spectra of **4a** in 1,2-dichloroethane without (a) and with (b) PS in solutions. The spectra of the two samples are very similar, thus the presence of PS has very little, if at all, influence on the self-assembly of PBI **4a**.

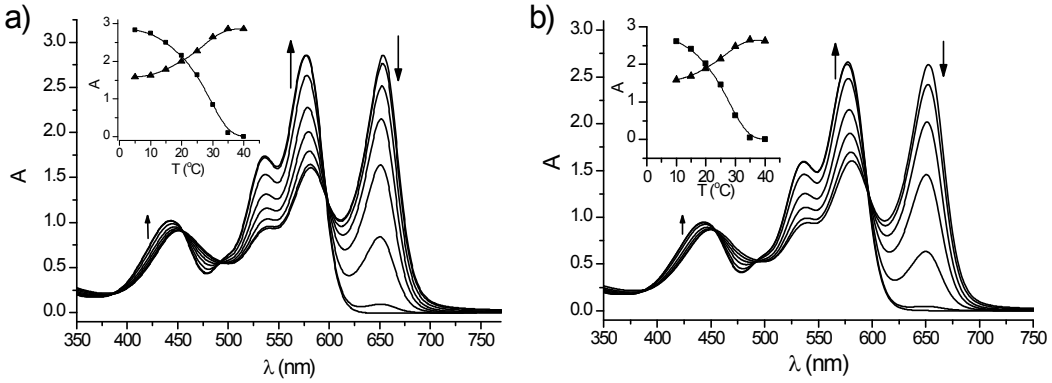

Fig. S2 (a) Temperature-dependent UV/vis spectra of **4a** (0.55 mg/mL, 6.7 × 10^{-4} M) in 1,2-dichloroethane from 5 to 40 °C in a 1 mm cell. (b) Temperature-dependent UV/vis spectra of **4a** (0.5 mg/mL, 6.1 × 10^{-4} M) in the presence of PS (20 mg/mL) in 1,2-dichloroethane from 10 to 40 °C in a 1 mm cell. Arrows indicate the spectral changes with increasing temperature, and insets show the changes of absorption at 651nm (■) and 578 nm (▲) upon increasing temperature in each case, respectively.

Towards many applications the formation of nanofibers in polymeric matrices is a requirement. Accordingly, we have assessed the self-assembly ability of PBI **4a** in a polymer matrix. For this purpose, a mixture of **4a** (0.5 mg/mL) and polystyrene (PS) (4.0 mg/mL) in 1,2-dichloroethane was studied by TEM. As evident from TEM images depicted in Figure S3a and b, nanofibers of PBI **4a** are indeed formed in the polymer matrix. Note that the difficult focusing on the nanofibers is due to a three-dimensional spatial distribution of fibers in the polymer matrix. The nanofibers wrapped by the polymer are not only on focusing plane. Further experiments were performed with a mixture of **4a** (0.5 mg/mL) and higher amounts of PS (20 mg/mL) in 1,2-dichloroethane. This mixture was heated

up to 70 °C to make a solution, which was then dropped onto a glass substrate for 3 min, followed by spin-coating under 4000 rpm and subsequently the film was subjected to AFM measurements. As shown in Figure 3c and 3d, impressive AFM images are obtained that reveal strong self-assembly ability of **4a** in the doped system. Nanofibers are readily formed, which come out to the surface of the polymer film in some regions and sink into the polymer matrix in other regions. The *in situ* formation of the nanofibers in concentrated PS solution confirms the strong self-assembly ability of **4a**. The temperature-dependent UV/vis absorption spectra of **4a** in 1,2-dichloroethane without and with PS indicated that the presence of PS has very small influence on the self-assembly of **4a** (Fig. S2).

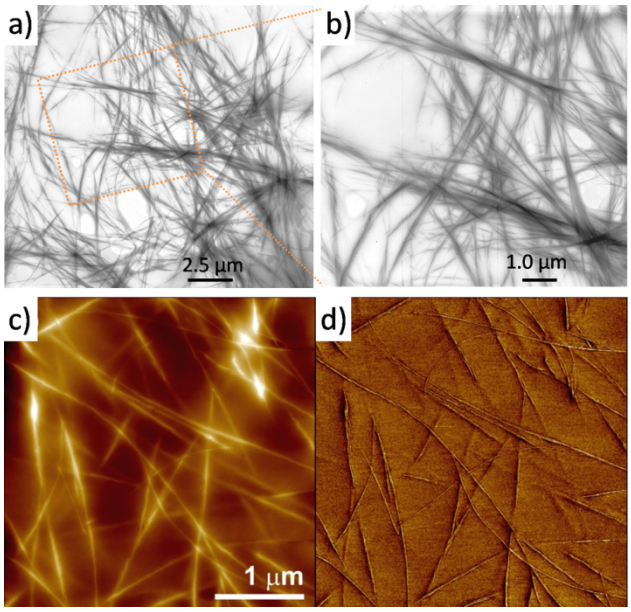

Fig. S3 (a), (b) TEM images of **4a** in PS matrix. PBI **4a** (0.5 mg/mL) and PS (4 mg/mL) were dissolved in 1,2-dichloroethane by gentle heating, then the mixture was put in an ice bath to form a gel. The samples for TEM were prepared by drop-casting from the suspension of shake-destroyed gel onto a carbon film. (c), (d) Height and phase AFM images of **4a** in PS matrix. The sample was prepared by drop-casting from a warm solution of **4a** (0.5 mg/mL) and PS (20 mg/mL) in 1,2-dichloroethane onto glass for 3 min, followed by spin-coating under 4000 rpm. The z scale is 60 nm (c).

5. FT-IR Spectrum of 4a

In IR spectrum (Fig. S4), the band at 1682 cm^{-1} was assigned to the stretching frequency of C=O with hydrogen-bonded carbonyl groups (C=O···H-N), while the band at 1702 cm^{-1} was assigned to the stretching frequency of free carbonyl groups (C=O).

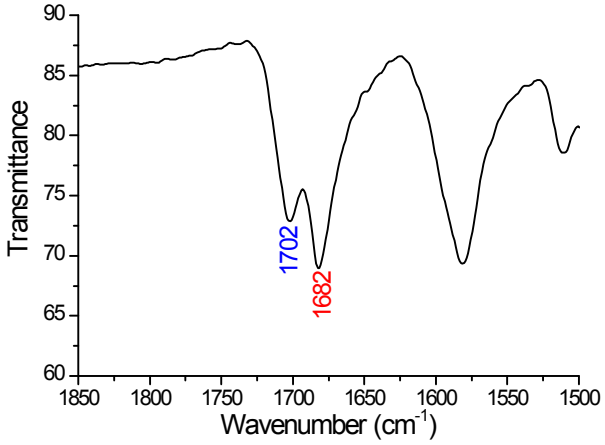

Fig. S4 IR spectrum of **4a** in the solid state at room temperature, measured on a Jasco FT/IR-410 instrument.

6. Selected Area Electron Diffraction (SAED) and Cross-Polarized Microscope Images of 4a Nanoneedles

PBI **4a** was dissolved in a mixture of chloroform and methanol (1:1) at a concentration of ~ 0.3 mg/mL. The solution was filled into a small vial that was placed in a big flask that contained a layer of methanol. The solvent exchange between the vial and the flask went slowly, and after several days very thin crystalline needle formed. For SAED studies these needles were suspended in ethanol, poured onto a carbon grid and mounted on a TEM sample holder. For cross-polarized microscopy studies the needles were dispersed in MCH and drop-cast onto a glass substrate. Figure S5 shows the results of the SAED studies. Figure S6 shows the images of the crystalline needles under cross-polarized microscope. From the image of Figure S6 we can see that the birefringence of the crystalline needles is minimal at a position parallel to the polarizer, while it is maximal when the needles are aligned at 45° to the direction of the polarizer.

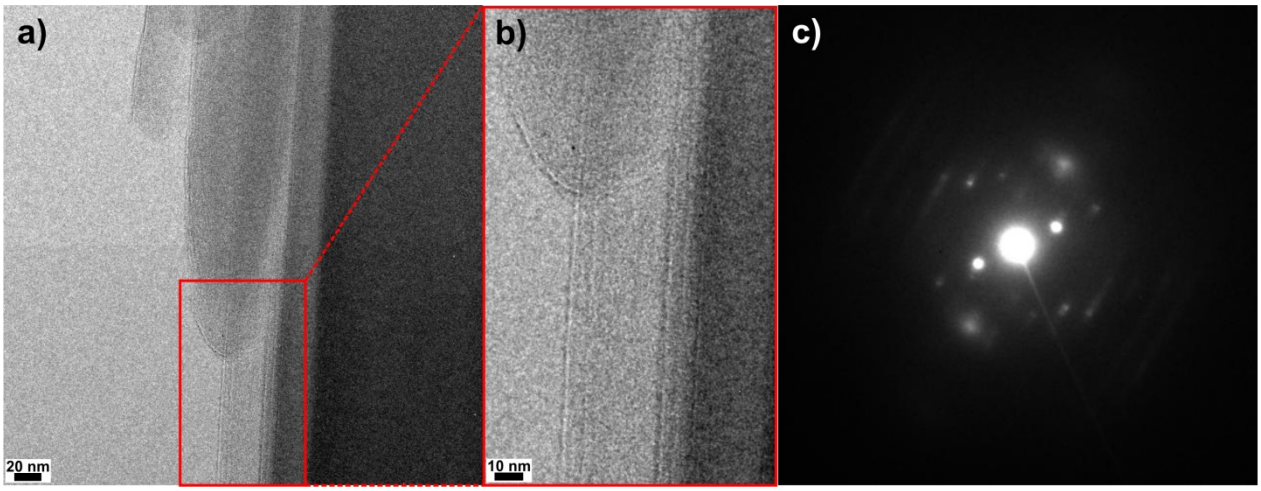

Fig. S5 TEM image of single crystalline needle of **4a** (a). The zoomed area (marked by red rectangle in image (a)) showed crystalline terraces (b). The SAED pattern depicted in image (c) confirmed the crystalline structure of needles **4a**.

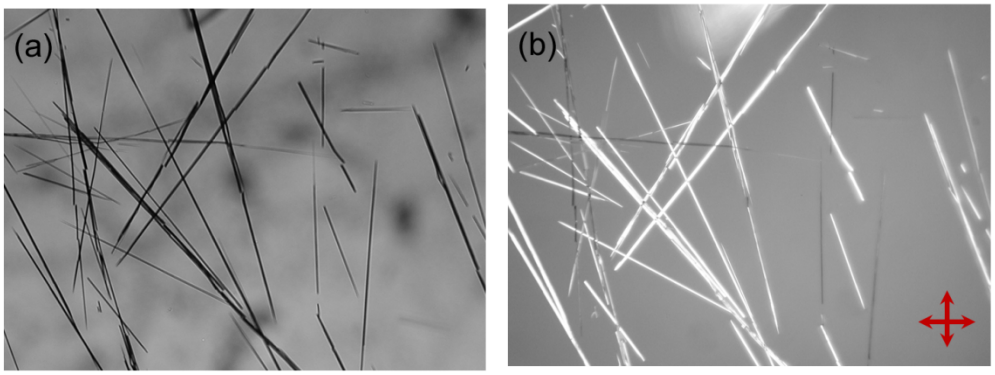

Fig. S6 Images of single crystalline needles of **4a** under cross-polarized microscope. (a) Taken in bright field. (b) Taken in dark field. The red double arrows indicate the directions of the polarizers.

7. Powder XRD studies and DSC Heating Scan of PBI 4a.

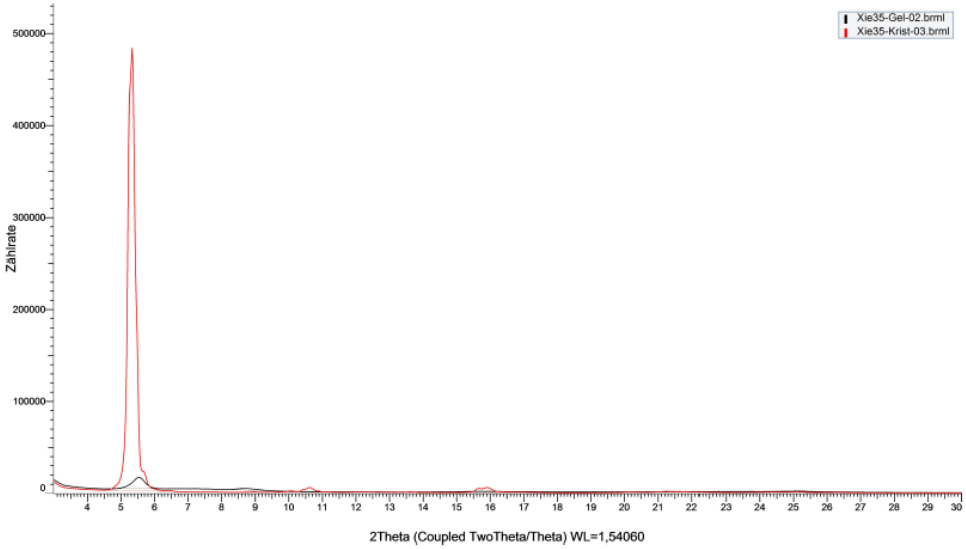

Fig. S7 Powder XRD diffraction data for PBI **4a** nanoneedles (red) and dried organogel fibers (black).

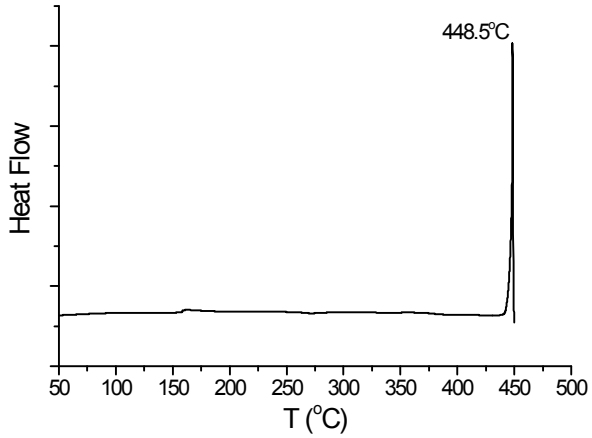

Fig. S8 DSC heating scan (10 K/min) for **4a**.

8. Quantum Chemical Calculations

To shed light on the molecular structure, in particular the orientation of the *ortho*-methylphenoxy groups attached to the bay positions of PBI dye **4a**, we performed quantum chemical calculations. In this approach, we first built up three starting structures of **4a** as schematically illustrated in Fig. S9. In these, based on the orientation of the methyl groups, the starting geometries are classified as outer-outer (I), inner-outer (II) or inner-inner (III). For all calculations the *M*-enantiomer was investigated as the situation for the *P*-enantiomer is the energetically the same.

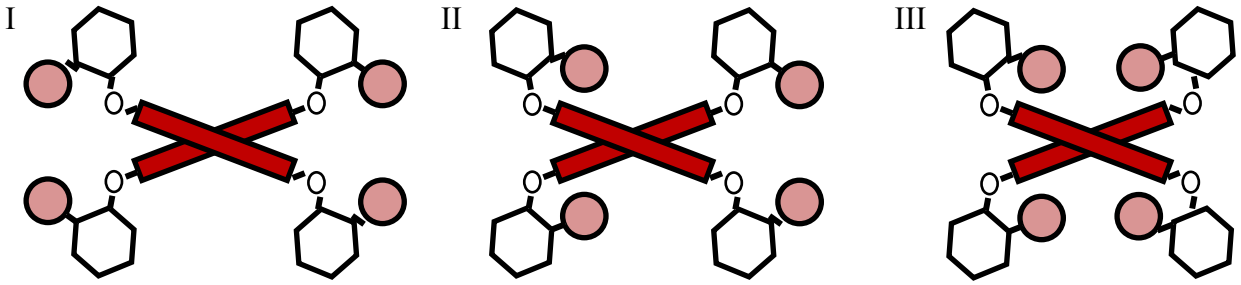

Fig. S9 Schematic illustrations of the starting structures for energy minimization of PBI **4a**: (I) outer-outer, (II) inner-outer and (III) inner-inner orientation of *ortho*-methylphenoxy substituents.

Subsequently, geometry optimizations with the force field OPLS-AA[S6] in Tinker 6.2[S7] and the more precise B3LYP functional[S8] with cost-efficient STO-3G basis sets[S9] in Gaussian 09[S10] were performed. From these calculations two important points can be seen for both methods. On the one hand, all three conformers I to III lead to different local energy minima as the initial orientations of the methyl substituents remain unchanged (Fig. S10). For energy-minimized conformation I the phenoxy groups remain oriented up- and downward, thereby shielding the perylene π-surfaces and prohibiting π-stacking with neighboring PBI molecules in aggregates or solid state materials. This situation is changed for energy-minimized conformations II and III: Here all four bay substituents are arranged to the flanks of the PBI core as a consequence of the repulsion of the methyl substituents to each other and to the perylene plane, and the attractive interactions between the phenyl moieties on both PBI sides (the distance between two ipso-carbon atoms of adjacent phenoxy groups is measured to be approx. 3.6 Å). Whilst for both of

these conformations the center of the PBI molecule still experiences some shielding by the methyl groups it appears now feasible that slipped π–stacks can be formed with other PBI molecules from the upper and lower side as illustrated in Figure 4.

I

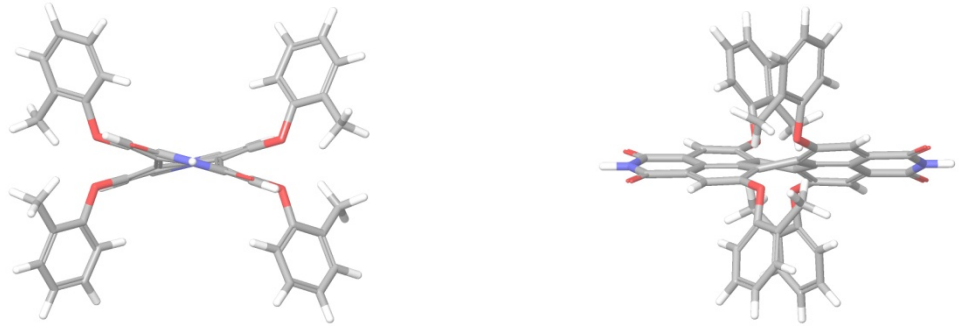

II

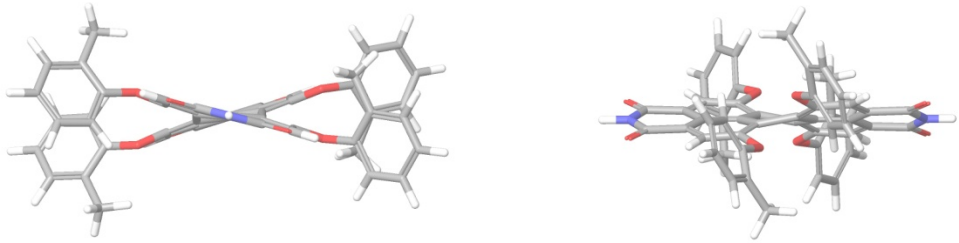

III

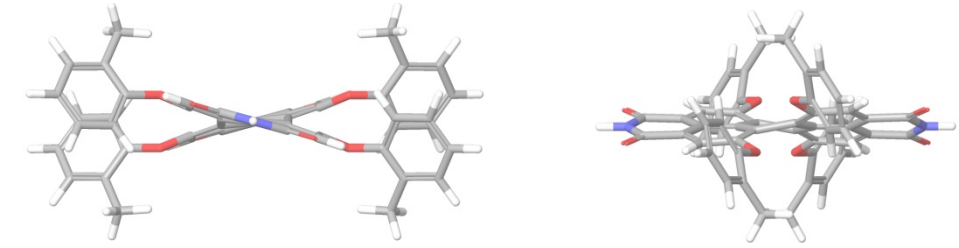

Fig. S10 Molecular structures of **4a** obtained by B3LYP/STO-3G geometry optimizations for conformations I, II and III; view along the N-N axis (left) and side view on the PBI scaffold (right).

The energy minimum for the inner-inner orientation (III) is the lowest and the energy of the inner-outer (II) is the highest according to OPLS-AA force field (Table S1). The relative energies of all three force field optimized systems are, however, only within 10 kJ/mol. For the more reliable B3LYP calculation, conformer III remains the one with the lowest energy and a strong increase of energy is observed for conformer I (47.2 kJ/mol).

Table S1 Relative energies[a)] of the three investigated conformations I, II and III after optimization with the stated methods.[b)]

	E (OPLS-AA)	*E* (B3LYP/STO-3G)
I	4.01	47.23
II	10.04	4.87
III	0	0

a) in kJ/mol. *b)* For energy-minimized molecular structures, see Figure S9.

Accordingly, we can conclude that the outer-outer orientation that cannot form phenyl-phenyl contacts due to the constraints imparted by the methyl groups is disfavored and should not be populated in significant amounts. The structurally and energetically similar conformations II and III (differences in OPLS-AA of 10.0 kJ/mol and in B3LYP/STO-3G of 4.9 kJ/mol) might, however, coexist in solution and accordingly it will depend on the packing energies and crystallization kinetics which conformation will prevail in supramolecular fibres or nanocrystals. These computational results are consistent with earlier experimental and theoretical studies on tetraphenoxy-substituted PBIs without methyl substituents[S11] where depending on the experimental conditions (solvent, temperature, packing forces) all of these conformations have been considered. It appears, however, that the *ortho*-methyl groups provide a clear bias to disfavor conformation I which is an important clue with regard to the solubility and self-assembly properties of **4a**. Thus, in contrast to conformation I, both conformations II and III enable the formation of hydrogen bond-directed slipped stack packing arrangements, leading to J-type excitonic coupling, either in one-dimensional string or in two-dimensional brickwall structures (Fig. 4). For simplicity, we chose the higher symmetry structure III (which is also the one of lowest energy according to both OPLS-AA and B3LYP). Because the observed fibers (Fig. 3) did not reveal any helicity we assume a unit cell of alternating *M*- and *P*-enantiomers which has been observed in a single crystal of a related bay-substituted PBI, i.e. octachloro-PBI.[S12]

9. ^{1}H and ^{13}C NMR Spectra

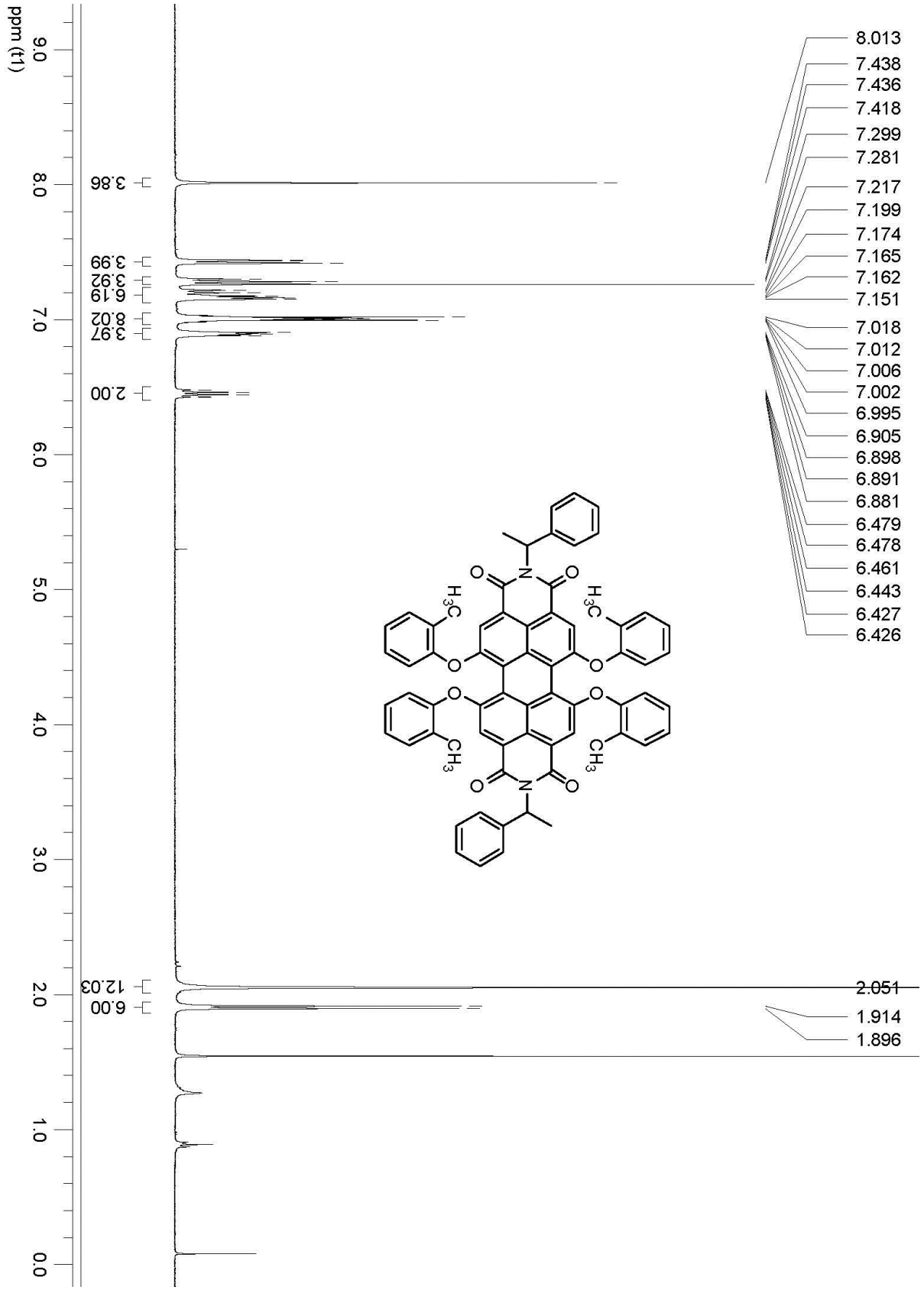

Fig. S11 ^{1}H NMR spectrum of compound **2a** in $CDCl_3$ at room temperature.

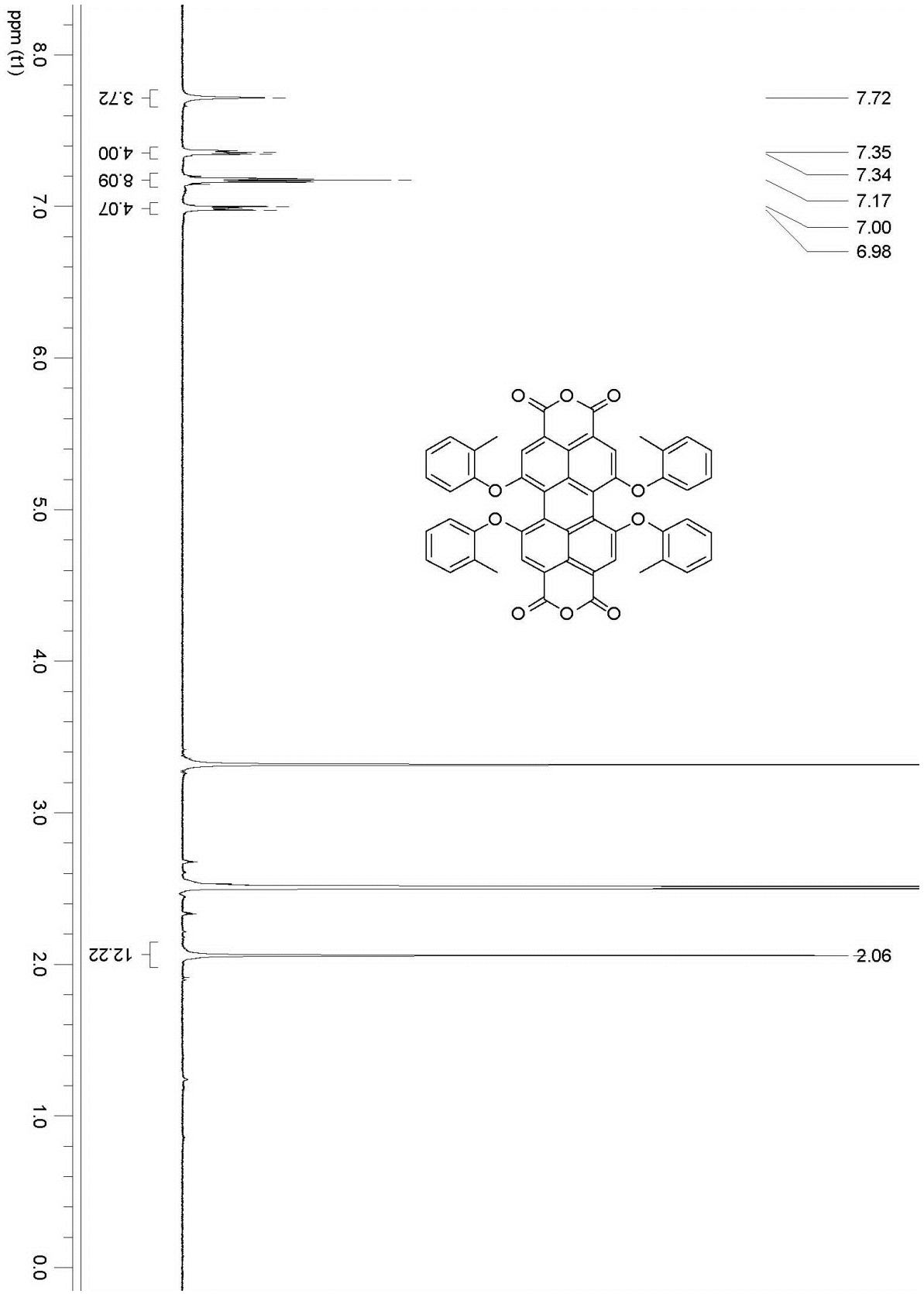

Fig. S12 ^{1}H NMR spectrum of compound **3a** in d_6-DMSO at room temperature.

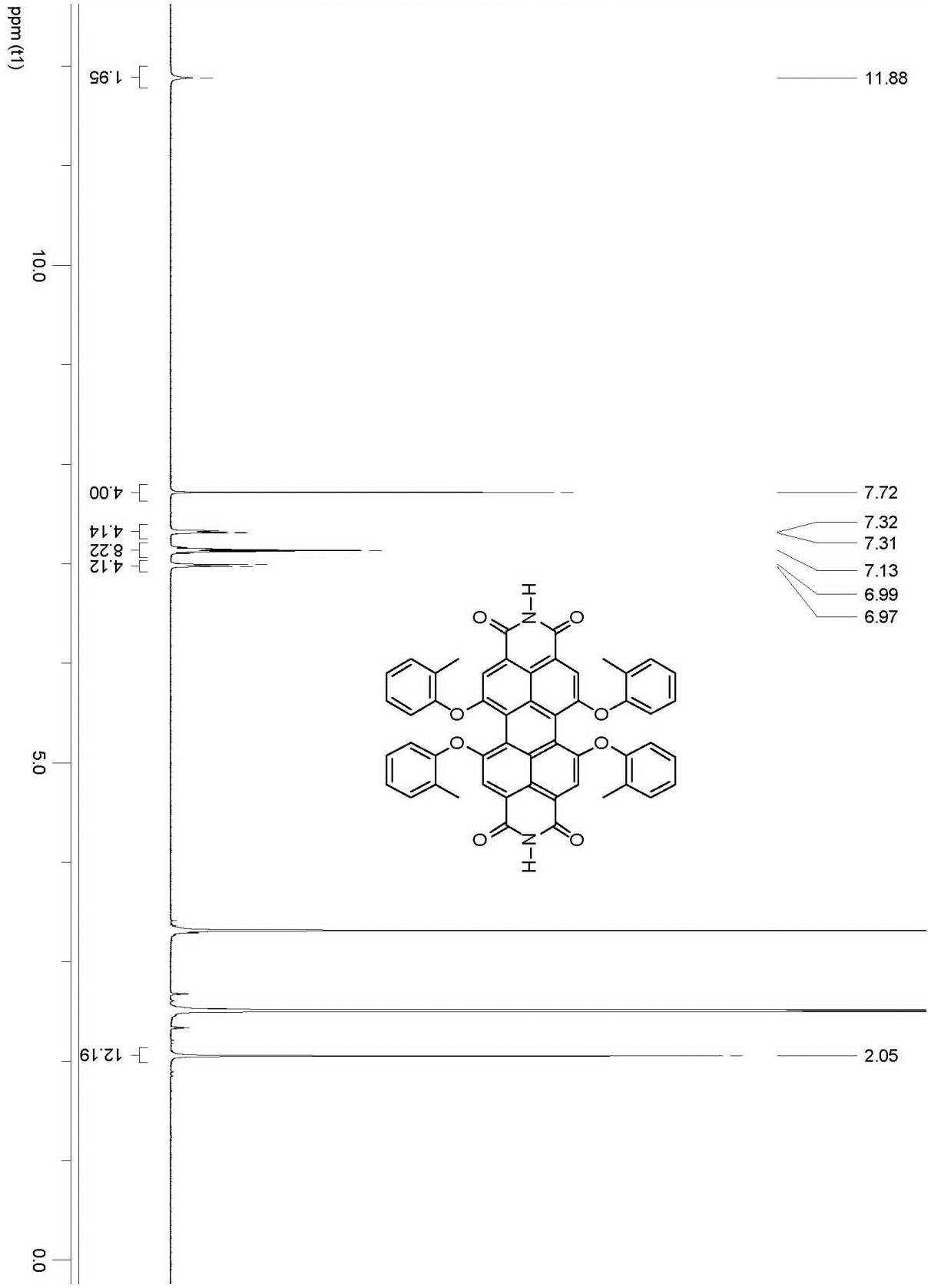

Fig. S13 ^{1}H NMR spectrum of compound **4a** in d_6-DMSO at room temperature.

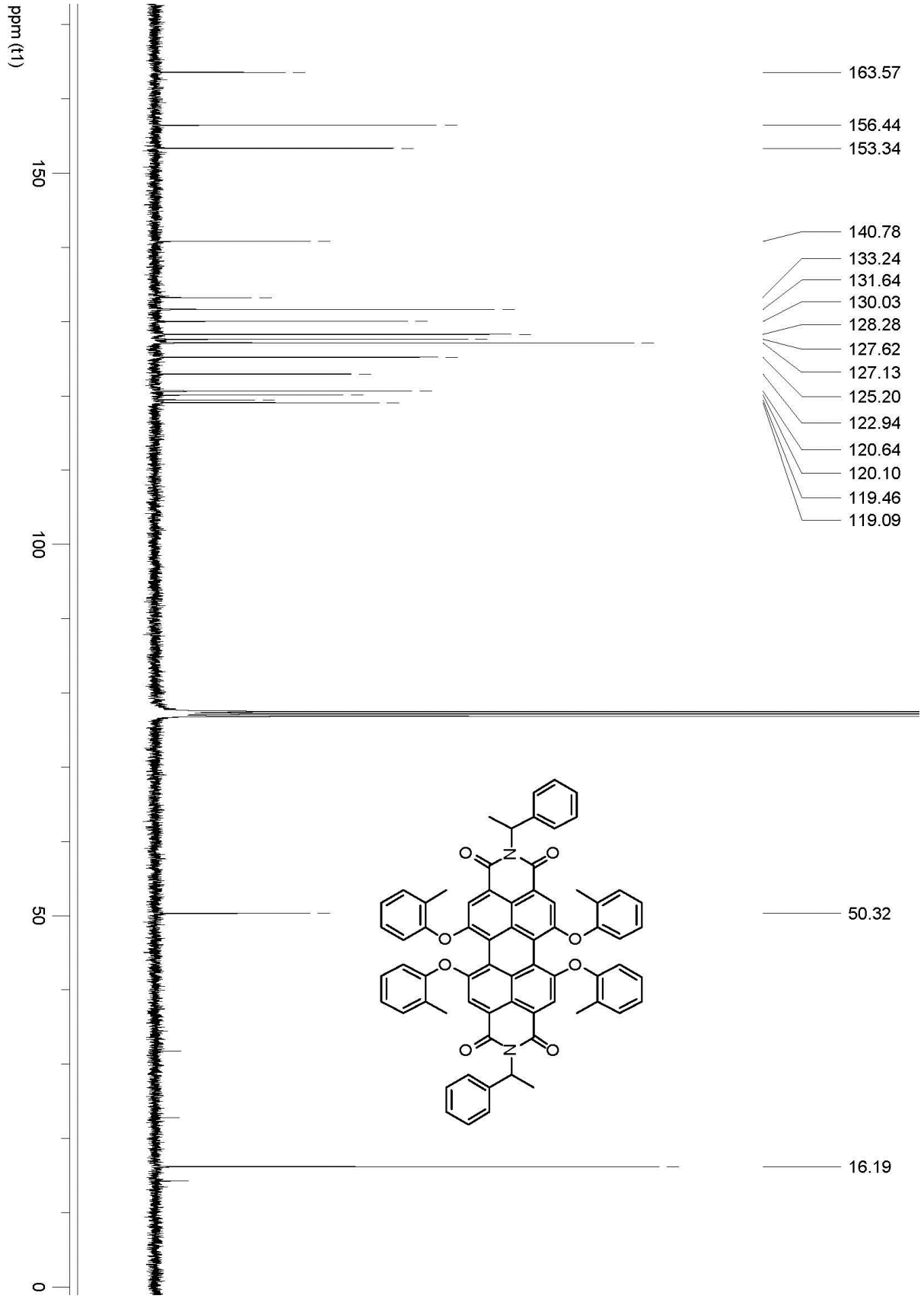

Fig. S14 ^{13}C NMR spectrum of compound **2a** in $CDCl_3$ at room temperature.

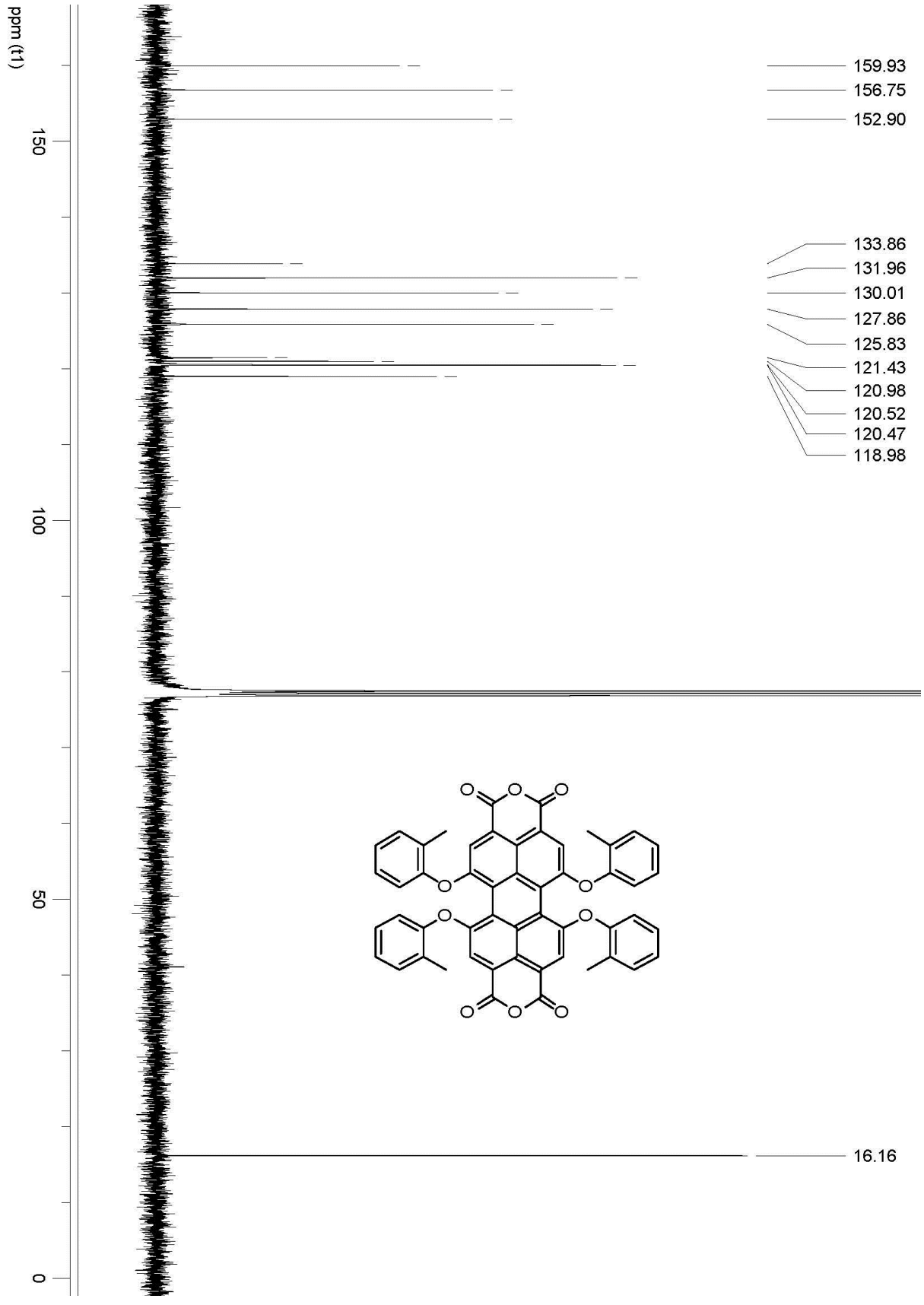

Fig. S15 ^{13}C NMR spectrum of compound **3a** in $CDCl_3$ at room temperature.

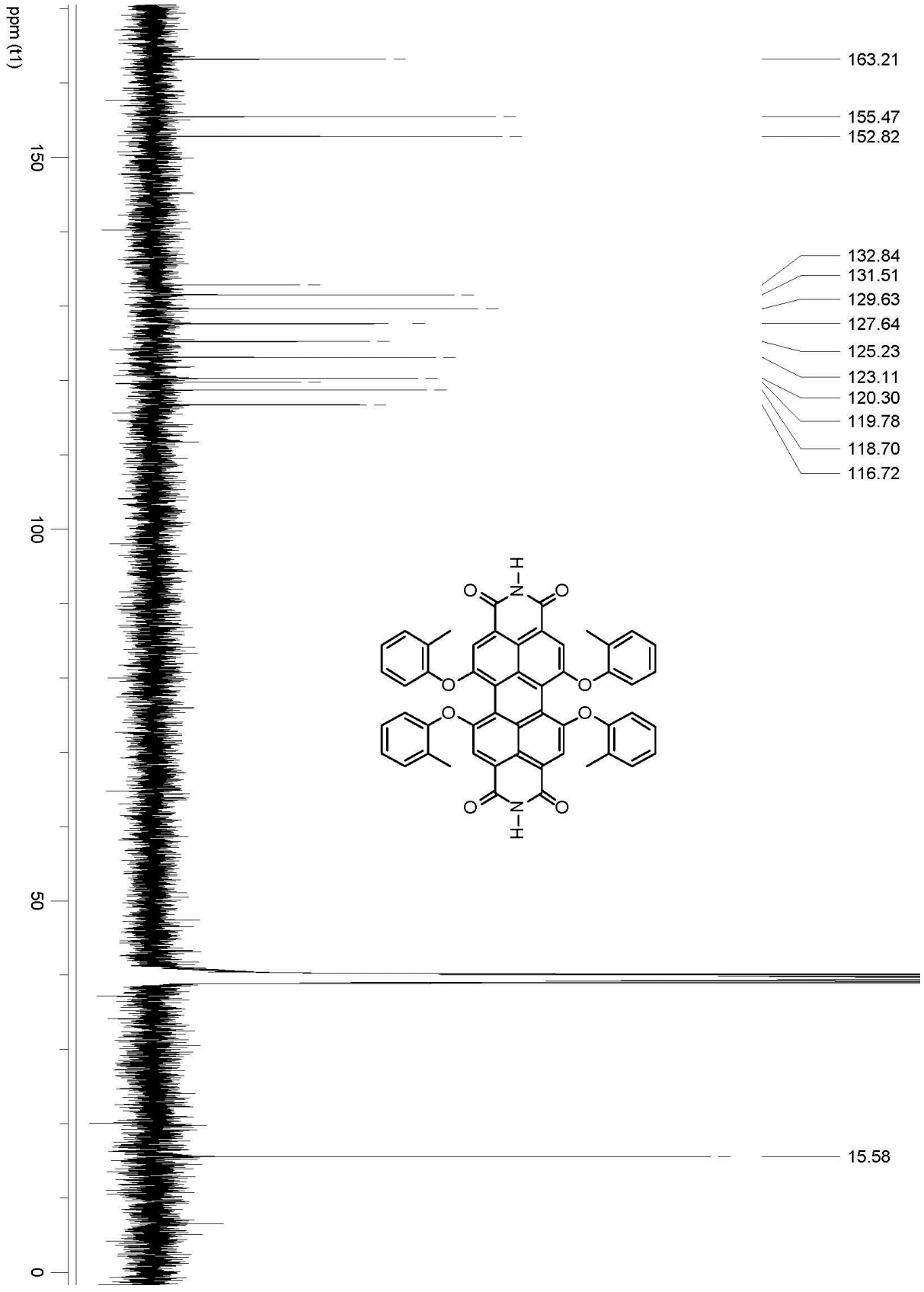

Fig. S16 ^{13}C NMR spectrum of compound **4a** in d_6-DMSO at room temperature.

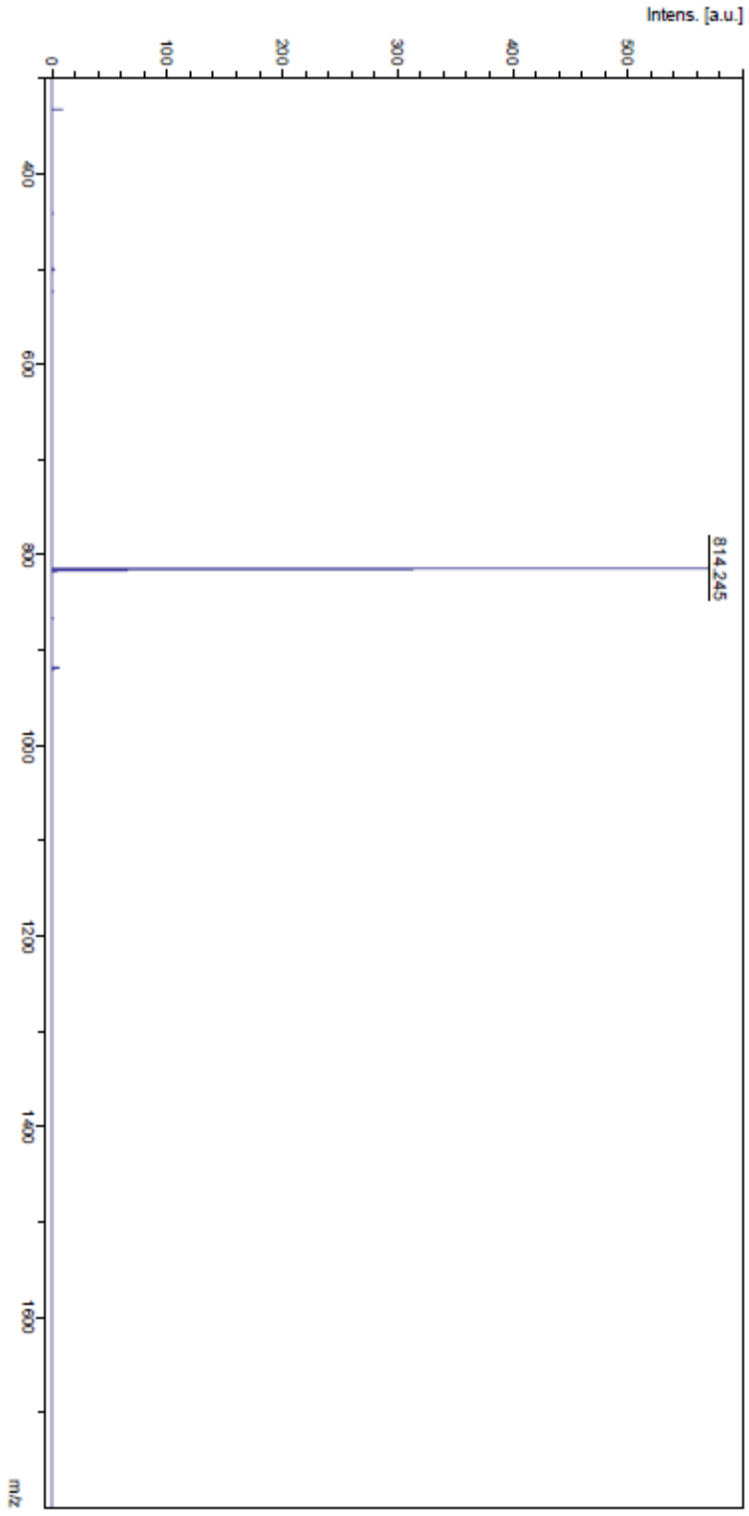

Fig. S17 MALDI-TOF spectrum of compound **4a** (positive mode, from chloroform using 2-[(2E)-3-(4-tert-butylphenyl)-2-methylprop-2-enylidene]malononitrile (DCTB) as a matrix).

9. Additional References

S1. G. Seybold and G. Wagenblast, *Dyes Pigm.*, 1989, **11**, 303-317.

S2. R. Gvishi, R. Reisfeld and Z. Burshtein, *Chem. Phys. Lett.*, 1993, **213**, 338-344.

S3. R. Sens and K. H. Drexhage, *J. Lumin.*, 1981, **24**, 709-712.

S4. F. Würthner, C. Thalacker, A. Sautter, W. Schärtl, W. Ibach and O. Hollricher, *Chem. Eur. J.*, 2000, **6**, 3871-3886.

S5. T. E. Kaiser, V. Stepanenko and F. Würthner, *J. Am. Chem. Soc*., 2009, **131**, 6719-6732.

S6. a) W. L. Jørgensen and J. Tirado-Rives, *J. Am. Chem. Soc*., 1988, **110**, 1657-1666; b) W. L. Jørgensen, D. S. Maxwell and J. Tirado-Rives, *J. Am. Chem. Soc*., 1996, **118**, 11225-11236.

S7. Tinker 6.2, J. W. Ponder, Saint Louis MO, 2013.

S8. a) A. D. Becke, *Phys. Rev. A*, **1988**, *38*, 3098-3100; b) C. Lee, W. Yang and R. G. Parr, *Phys. Rev. B*, **1988**, *37*, 785-789.

S9. a) W. J. Hehre, R. F. Stewart and J. A. Pople, *J. Chem. Phys*., **1969**, *51*, 2657-2664; b) J. B. Collins, P. v. R. Schleyer, J. S. Binkley and J. A. Pople, *J. Chem. Phys.*, **1976**, *64*, 5142-5151.

S10. Gaussian 09, Revision B.01, M. J. Frisch, G. W. Trucks, H. B. Schlegel, G. E. Scuseria, M. A. Robb, J. R. Cheeseman, G. Scalmani, V. Barone, B. Mennucci, G. A. Petersson, H. Nakatsuji, M. Caricato, X. Li, H. P. Hratchian, A. F. Izmaylov, J. Bloino, G. Zheng, J. L. Sonnenberg, M. Hada, M. Ehara, K. Toyota, R. Fukuda, J. Hasegawa, M. Ishida, T. Nakajima, Y. Honda, O. Kitao, H. Nakai, T. Vreven, J. A. Montgomery, Jr., J. E. Peralta, F. Ogliaro, M. Bearpark, J. J. Heyd, E. Brothers, K. N. Kudin, V. N. Staroverov, T. Keith, R. Kobayashi, J. Normand, K. Raghavachari, A. Rendell, J. C. Burant, S. S. Iyengar, J. Tomasi, M. Cossi, N. Rega, J. M. Millam, M. Klene, J. E. Knox, J. B. Cross, V. Bakken, C. Adamo, J. Jaramillo, R. Gomperts, R. E. Stratmann, O. Yazyev, A. J. Austin, R. Cammi, C. Pomelli, J. W. Ochterski, R. L. Martin, K. Morokuma, V. G. Zakrzewski, G. A. Voth, P. Salvador, J. J. Dannenberg, S. Dapprich, A. D. Daniels, O. Farkas, J. B. Foresman, J. V. Ortiz, J. Cioslowski and D. J. Fox, Gaussian, Inc., Wallingford CT, 2010.

S11. E. Fron, G. Schweitzer, P. Osswald, F. Würthner, P. Marsal, D. Beljonne, K. Müllen, F. C. De Schryver and M. Van der Auweraer, *Photochem. Photobiol. Sci.* **2008**, *7*, 1509-1521.

S12. M. Gsänger, J. H. Oh, M. Könemann, H. W. Höffken, A.-M. Krause, Z. Bao and F. Würthner, *Angew. Chem. Int. Ed.,* **2010**, *49*, 740-743.